Biased Brownian motion as a mechanism to facilitate nanometer-scale exploration of the microtubule plus end by a kinesin-8

Yongdae Shin[a,1], Yaqing Du[b,1], Scott E. Collier[b], Melanie D. Ohi[b], Matthew J. Lang[c,d,2,3], and Ryoma Ohi[b,2,3]

[a]Department of Mechanical Engineering, Massachusetts Institute of Technology, Cambridge, MA 02139; [b]Department of Cell and Developmental Biology, Vanderbilt University Medical Center, Nashville, TN 37232; [c]Department of Chemical and Biomolecular Engineering, Vanderbilt University, Nashville, TN 37235; and [d]Department of Molecular Physiology and Biophysics, Vanderbilt University, Nashville, TN 37235

Edited by J. Richard McIntosh, University of Colorado, Boulder, CO, and approved June 11, 2015 (received for review January 6, 2015)

Kinesin-8s are plus-end–directed motors that negatively regulate microtubule (MT) length. Well-characterized members of this subfamily (Kip3, Kif18A) exhibit two important properties: (*i*) They are "ultraprocessive," a feature enabled by a second MT-binding site that tethers the motors to a MT track, and (*ii*) they dissociate infrequently from the plus end. Together, these characteristics combined with their plus-end motility cause Kip3 and Kif18A to enrich preferentially at the plus ends of long MTs, promoting MT catastrophes or pausing. Kif18B, an understudied human kinesin-8, also limits MT growth during mitosis. In contrast to Kif18A and Kip3, localization of Kif18B to plus ends relies on binding to the plus-end tracking protein EB1, making the relationship between its potential plus-end–directed motility and plus-end accumulation unclear. Using single-molecule assays, we show that Kif18B is only modestly processive and that the motor switches frequently between directed and diffusive modes of motility. Diffusion is promoted by the tail domain, which also contains a second MT-binding site that decreases the off rate of the motor from the MT lattice. In cells, Kif18B concentrates at the extreme tip of a subset of MTs, superseding EB1. Our data demonstrate that kinesin-8 motors use diverse design principles to target MT plus ends, which likely target them to the plus ends of distinct MT subpopulations in the mitotic spindle.

kinesin-8 | Kif18B | microtubule | EB1 | mitosis

Kinesins are microtubule (MT)-dependent motors that fulfill a wide range of cellular functions. By ferrying cargos through cytoplasm, transport motors help to organize the contents of a cell. MT regulatory kinesins, on the other hand, modulate the polymerization state of MT ends, thereby altering the architecture and function of MT-based structures. Kinesin-8s, motors that regulate diverse cellular processes, ranging from spindle positioning in yeast (1) to chromosome alignment (2–4) and motile cilia length in animal cells (5), exhibit features of both transport and MT-regulating kinesins (6). Yeast Kip3, the first well-studied kinesin-8, and human Kif19 are plus-end–directed motors that depolymerize MTs once they reach the plus end (5, 7, 8). Human Kif18A, also a plus-end–directed motor, does not depolymerize MTs but instead causes their plus ends to pause, a state wherein tubulin subunits neither add to nor release from the plus end (9–11). Kif18B, a third human kinesin-8, limits the length of astral MTs in the mitotic spindle (12, 13) and has been reported to do so by recruiting the MT depolymerizing kinesin-13 MCAK to MT plus ends (13). Whether Kif18B also regulates MT plus-end dynamics is unclear, but recent work showing that the motor domain of Kif18B can substitute for that of Kif18A (14) suggests that this may be the case.

Among the MT-regulating kinesins, Kip3 and Kif18A are unique in that they are capable of regulating MT dynamics in a length-dependent manner. A major factor thought to underlie this property is that Kip3 and Kif18A are ultraprocessive motors (8, 10, 15), preferentially concentrating them at the ends of long MTs. Ultraprocessivity is enabled, at least in part, by MT binding of the nonmotor C-terminal tail domains of Kif18A and Kip3, an activity that tethers the motors to the MT track (10, 15, 16). In addition, Kip3 and Kif18A exhibit long dwell times at MT plus ends (8–10). Combined, these properties enrich Kip3 and Kif18A onto long, stable MTs such as those attached to kinetochores (K-MTs) during mitosis (2, 3) and are therefore well matched to their function in driving chromosome movement toward the spindle equator (2–4, 17).

Whether the paradigm set by Kip3 and Kif18A will apply to all kinesin-8 motors is unclear. Kif18B localizes to astral MT plus ends, but does so in a manner that requires the plus-end tracking protein EB1 (12, 13). Heightened processivity is therefore not required to target Kif18B to MT plus ends, and it remains unclear how the motor employs plus-end–directed motility. Using a combination of high-resolution single-molecule and cellular assays, we show that Kif18B is not ultraprocessive like Kip3 and Kif18A and that it uses a hybrid form of motility involving both diffusion and plus-end–directed motility. Diffusion is promoted by a second MT-binding site located in the tail of Kif18B, a function distinct from the processivity-promoting MT-binding tail of Kif18A. We also demonstrate that Kif18B targets the extreme MT plus end, a region spatially distinct from that recognized by EB1. Kif18B thus uses a suite of unique biophysical properties to target the plus ends of astral MTs.

Significance

The cellular distributions of kinesins are defined in part by their intrinsic biophysical properties. The well-characterized kinesin-8s, for example, translocate exceptionally long distances on a microtubule track, concentrating them at plus ends of long, stable microtubules. Kif18B, a little-studied kinesin-8, targets the plus ends of fast-growing, short-lived microtubules by binding the plus-end tracking protein EB1. Whether ultraprocessivity is conserved among kinesin-8s is thus unclear. Here, we show that Kif18B is not ultraprocessive and that the motor switches frequently between diffusive and directed modes of motility. Our work identifies properties of Kif18B that may have optimized the motor to explore the ∼1-μm domain of microtubule plus ends and show that biophysical motor properties cannot be generalized within any one kinesin subfamily.

Author contributions: Y.S., Y.D., M.J.L., and R.O. designed research; Y.S., Y.D., and S.E.C. performed research; Y.S., Y.D., and S.E.C. contributed new reagents/analytic tools; Y.S., Y.D., S.E.C., and M.D.O. analyzed data; and Y.S., M.J.L., and R.O. wrote the paper.

The authors declare no conflict of interest.

This article is a PNAS Direct Submission.

[1]Y.S. and Y.D. contributed equally to this work.

[2]M.J.L. and R.O. contributed equally to this work.

[3]To whom correspondence may be addressed. Email: ryoma.ohi@vanderbilt.edu or matt.lang@vanderbilt.edu.

This article contains supporting information online at www.pnas.org/lookup/suppl/doi:10.1073/pnas.1500272112/-/DCSupplemental.

Results

Kif18B Has Motile Properties Distinct from Other Kinesin-8s. To investigate the motile properties of single Kif18B molecules on the MT lattice, we expressed and purified GFP-tagged full-length Kif18B (GFP-Kif18B-FL), using the insect cell expression system (Fig. S1*A*). Unless indicated otherwise, all assays to characterize Kif18B in vitro were performed in BRB80. In conventional MT gliding assays, GFP-Kif18B-FL moves polarity-marked GMPCPP MTs with their dim plus ends trailing, as expected for a plus-end–directed motor (Fig. S1*B*, speed = 0.089 ± 0.003 μm·s^{-1}). The oligomeric nature of GFP-Kif18B-FL was examined by comparing single-molecule intensity distributions of individual GFP-Kif18B-FL, dimeric GFP-Kif18A-FL (10), and isolated GFP molecules (Fig. S1 *C*–*E*). The mean intensity of surface-bound GFP-Kif18B-FL was similar to that of GFP-Kif18A-FL and twice that of single GFP, demonstrating that GFP-Kif18B-FL exists as a homodimer in solution. To examine the movement of single Kif18B molecules on the MT lattice, 1 nM of GFP-Kif18B-FL was introduced into a flow cell with surface-immobilized MTs and imaged with total internal reflection fluorescence (TIRF) microscopy (Fig. 1*A*). In the presence of 1 mM ATP, fluorescent spots appeared on the MT lattices, moved, and disappeared (Fig. 1*B*). In a small number of long binding events, intensities of fluorescent spots showed two-step photobleaching as expected for dimeric proteins (Fig. S1*F*).

In contrast to the ultraprocessive Kip3 and Kif18A motors, which translocate on MTs for up to 12 μm (8, 10, 15), single Kif18B motors exhibited only modest processivity with a mean run length of 0.74 ± 0.22 μm (mean ± SEM; n = 106; Fig. 1*C*) in the presence of BRB80. In fact, only a small fraction of Kif18B motors reached the MT plus end. After arriving at the end, Kif18B was not stationary but exhibited brief back-and-forth movements (Fig. 1*D*). This saltatory behavior is distinct from that of Kip3, which remains stably bound to MT plus ends (18). Given that our ability to localize spots was limited to ∼25 nm (*Materials and Methods*), we speculated that Kif18B could move backward more frequently than observable by tracking fluorescent spots.

To observe movements of Kif18B with higher spatial and temporal resolution, we attached a 440-nm-diameter polystyrene bead to the tail of Kif18B (*Materials and Methods*) and imaged its motion with differential interference contrast (DIC) microscopy (Fig. 1*E*) (19). To ensure that MT interactions were being mediated through single molecules of Kif18B, the Kif18B motor-to-bead ratio was adjusted so that fewer than 50% of beads tested on MTs showed binding (20). Using video tracking, positions of the Kif18B-bound beads were localized with a spatial resolution of ∼6 nm at a time resolution of 33 ms (Fig. S2*A*). Motile properties of Kif18B-bound beads were consistent with those observed with single-molecule fluorescence tracking (Fig. S2*B*). Similar back-and-forth motions were observed in the video-tracking assay when the Kif18B bead reached the MT end (Fig. 1*F*). Short pauses at the MT end were flanked by frequent back-and-forth movements spanning from tens of nanometers to several hundred nanometers (the nature of these backward motions is discussed below). Because the lengths of individual protofilaments vary at the MT plus ends (21), we conservatively defined a MT end as encompassing a 50-nm zone from the maximum displacement observed. Kif18B dwelled only transiently at the MT plus end with an average dwell time of 1.42 ± 0.57 s (mean ± SEM; n = 38; Fig. 1*G*).

Kif18B Switches Between Directed Motion and Diffusion. Although the general movement of individual Kif18B molecules was clearly unidirectional, frequent backward motions were observed (Fig. 2*A*), suggesting that Kif18B motility is punctuated by periods of diffusive motion. To address this possibility, we performed mean-squared

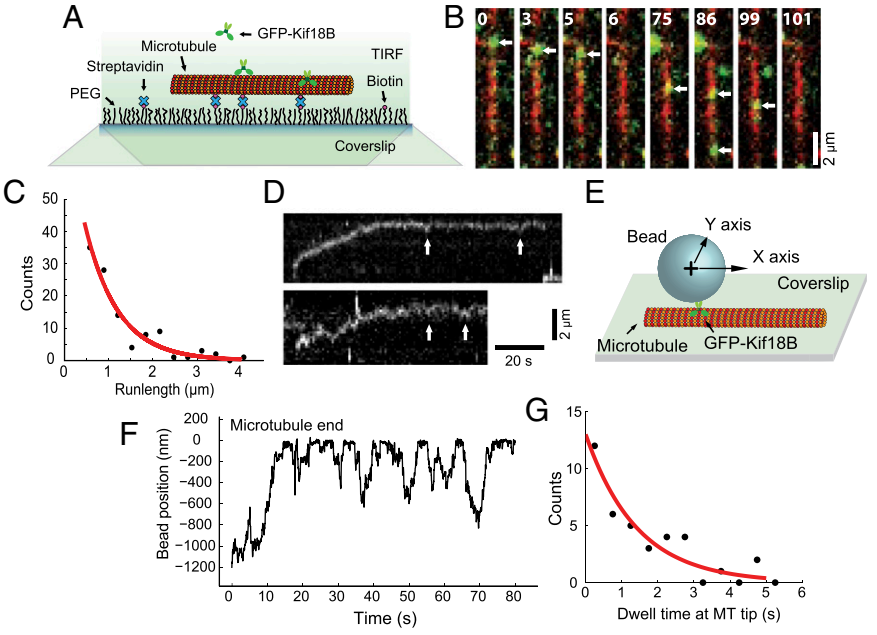

Fig. 1. Single-molecule analysis of Kif18B motility. (*A*) Single-molecule TIRF assay for Kif18B. Dilute GFP-Kif18B in solution is allowed to interact with a MT anchored to a glass coverslip via streptavidin–biotin linkages. TIRF microscopy is used to track individual molecules of GFP-Kif18B. (*B*) Sequential frames of a GFP-Kif18B-FL (green) video showing moderate processivity. Motility of single GFP-Kif18B-FL molecules on a MT (red) is marked by white arrows. Elapsed time is reported in seconds (s). (*C*) Run-length distribution of GFP-Kif18B-FL in 1 mM ATP. The red curve is a single exponential fit to the data with a fitting parameter, 0.74 ± 0.22 μm. n = 106. (*D*) Examples of kymographs showing back-and-forth movements of Kif18B at the MT end. Regions of such movements are marked by white arrows. (*E*) Video-tracking assay for Kif18B. GFP-Kif18B-FL is specifically linked to a bead using a pentahistidine antibody and the position of the bead is monitored using cross-correlation. (*F*) Example raw trace of a Kif18B-coated bead near the MT end. Frequent back-and-forth movements are evident. The zero position is an average of the 100 largest values observed in the trace. (*G*) Dwell time distribution of Kif18 at the MT end. The red curve is a single exponential fit to the data with a fitting parameter, 1.42 ± 0.57 s. n = 38.

displacement (MSD) (Fig. S3) analysis on GFP-Kif18B-FL motility trajectories in the presence of ATP. Kif18B displacement was best fit with a model incorporating both diffusion and directed motion parameters and yielded a diffusion coefficient, D, of 0.01 ± 0.001 $\mu m^{-2} \cdot s^{-1}$ and a velocity, v, of 0.052 ± 0.003 $\mu m \cdot s^{-1}$ (Fig. 2*B*). These values were used to compute a randomness parameter, r (= $2D/vd$, where d is the step size of the motor, here assumed to be 8 nm), which describes the extent of stochastic character in the stepping of motor proteins (22–24). For a motor whose motility is tightly coupled to ATP hydrolysis, r approaches 1; for example, kinesin-1/Kif5C has an r of 0.77 (25) whereas Cin8 and Eg5, which show both directional stepping and diffusion, exhibit an r of 73 and 13.7, respectively (26, 27). Our data indicate that for Kif18B, $r = 50$, consistent with the notion that it toggles between diffusion and directed modes of motility. In contrast to motility in the presence of ATP, single-molecule fluorescence tracking measurements in ADP-only containing buffers yielded purely diffusive movement with D = 0.015 ± 0.001 $\mu m^{-2} \cdot s^{-1}$. ATP hydrolysis is thus required for Kif18B's directed motility (Fig. 2 *C* and *D*).

We further examined Kif18B motility on the MT lattice, using high-resolution video tracking to define the fraction of time that Kif18B spends diffusing relative to moving in a directed manner. Consistent with fluorescence tracking, Kif18B-bound beads showed transient directional motions flanked by diffusive phases (Fig. 2*F*). As a control, we examined movements exhibited by kinesin-1, which is known to undergo smooth unidirectional translocation (Fig. 2*E*) (28). To objectively identify periods of transient directed stepping from diffusion, we used an automated algorithm based on the fact that velocity vectors are highly correlated for directed motion but uncorrelated for diffusion (Fig. 2*H*) (29). Because diffusion can occasionally generate motions appearing to be directed during short time periods, we implemented criteria for selecting directed motion regions such that the probability of falsely including diffusion events would be less than 5% (*Materials and Methods*). If the motor switches between directional stepping and diffusion, the instantaneous velocity during the directional phase is expected to be higher than the overall mean velocity. Furthermore, the ratio of the overall to instantaneous velocity must be equal to the temporal fraction of the directed phase because pure diffusion shows zero net movement (30). Indeed, directional phases we identified had a much larger slope than the overall plot of position vs. time (Fig. 2*G*). A model with only directional motion fits well the MSD calculated using detected directed phases, resulting in the

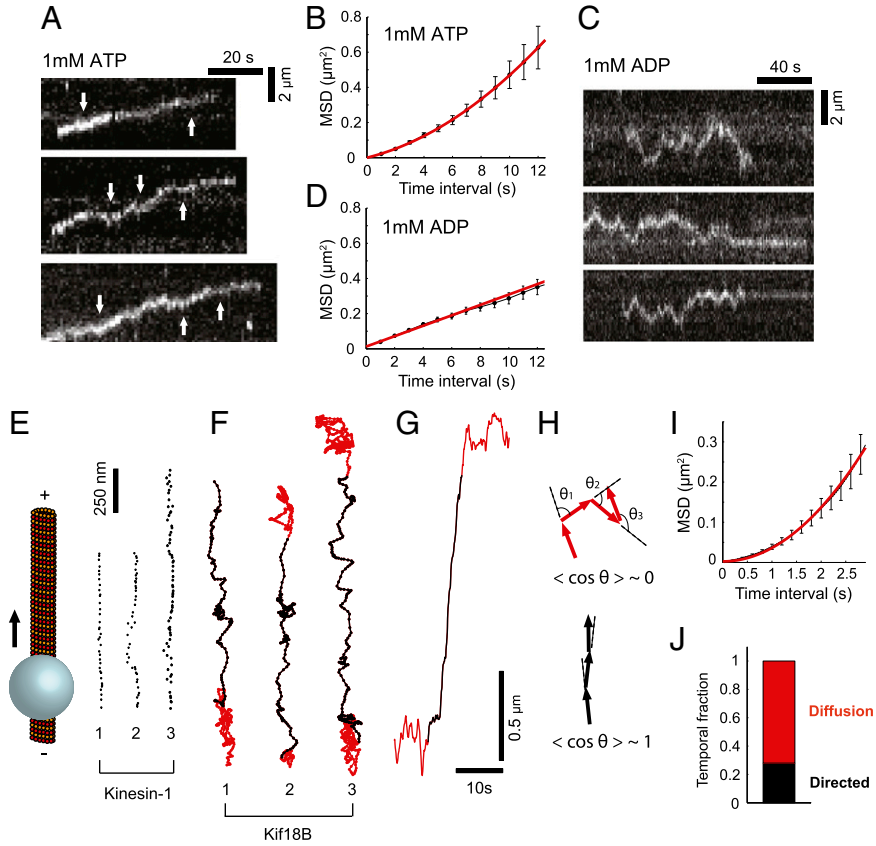

Fig. 2. Kif18B exhibits directed and diffusive modes of movement. (*A*) Representative kymographs of GFP-Kif18B-FL depicting two modes of motility (diffusive and directed motion) in the presence of 1 mM ATP. Examples of backward motion are indicated by white arrows. (*B*) Mean-squared displacement (MSD) of GFP-Kif18B-FL in 1 mM ATP. The red curve is a fit to MSD = $v^2\tau^2 + 2D\tau$ + offset, v = 0.052 ± 0.003 μm/s and D = 0.01 ± 0.001 μm^2/s. Error bars represent the SEM of the squared displacement values. n = 98. (*C*) Representative kymographs of GFP-Kif18B-FL showing diffusive movements in 1 mM ADP. (*D*) MSD of GFP-Kif18B-FL in 1 mM ADP. The red line is a fit to MSD = $2D\tau$ + offset, D = 0.015 ± 0.001 μm^2/s. Error bars represent the SEM of the squared displacement values. n = 78. (*E*) Example 2D raw trajectories of Kinesin-1 on MT (*Right*) tracked with the video tracking. Traces are plotted on top–down view and the motility is upward (*Left*). (*F*) Example 2D trajectories of Kif18B obtained by video tracking. Data were 10-frame moving averaged. Different colors denote diffusion (red) and directed motion (black) detected using a computer algorithm (*Materials and Methods*). (*G*) Position vs. time curve for trace 3 in *F*. The instantaneous velocity is much higher than the average velocity. (*H*) Velocity vectors are highly correlated for directed motion (*Lower*, black) but uncorrelated for diffusion (*Upper*, red). Thus, angles (θ) between adjacent velocity vectors remain very small for directed motion along the trajectory but they are randomly distributed in the case of diffusion. (*I*) MSD calculated with transient directed phases. The red curve is a fit to MSD = $v^2\tau^2$ + offset, v = 0.183 ± 0.002 μm/s. (*J*) Temporal fraction of Kif18B in each motility mode. Kif18B spends 72% of time in diffusion (red) while associating with the MT lattice.

instantaneous velocity during the directional stepping of 0.183 ± 0.002 μm·s^{-1} (Fig. 2*I*). A large difference between overall velocity and instantaneous velocity indicates that Kif18B spends a significant fraction of time (72%) in the diffusive mode during its association with MTs (Fig. 2*J*).

Diffusion can also account for the observed back-and-forth motions at the MT plus end (Fig. 1 *D* and *F*). To explore this possibility, we manually chose backward and forward portions separately in the video-tracked trace and performed MSD analyses for each type of movement (Fig. S4). The MSD calculated from backward motions increased linearly with D = 0.016 ± 0.001 μm^{-2}·s^{-1}, confirming that diffusion of Kif18B gives rise to backward motions at the MT tip. Notably, the diffusion constant in backward motions is very close to that measured for the diffusive motion in the presence of 1 mM ADP (Fig. 2*D*). In forward motions, the initial slope of MSD was similar to that from backward motions but MSD showed deviation from the linear fit for longer time intervals likely due to the presence of directed stepping.

The Kif18B Tail Modulates Motility Mode Switching of the Motor Heads. Because the C-terminal tail domain of Kif18A contains a second MT-binding site, we reasoned that the Kif18B tail might

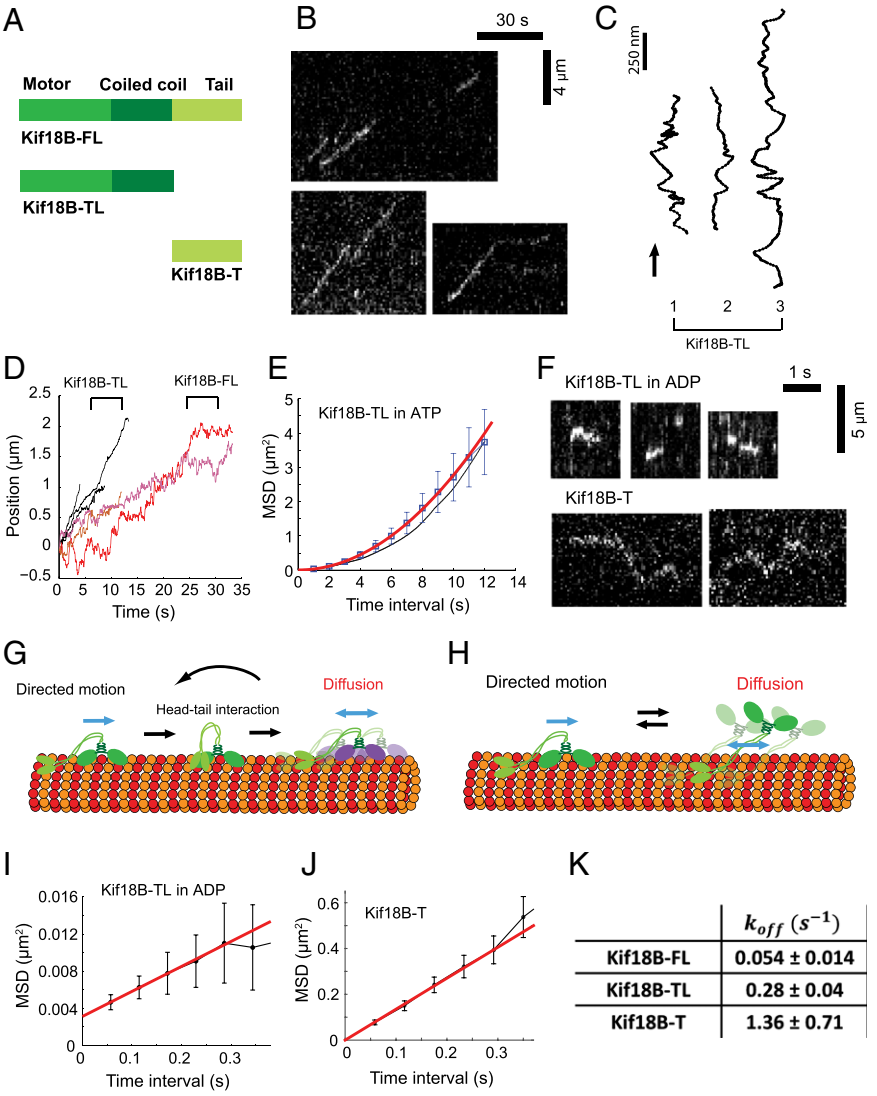

	k_{off} (s^{-1})
Kif18B-FL	0.054 ± 0.014
Kif18B-TL	0.28 ± 0.04
Kif18B-T	1.36 ± 0.71

Fig. 3. The tail domain permits the switching of motility mode in Kif18B. (*A*) Schematic diagrams of three Kif18B constructs used in this study. (*B*) Representative kymographs of tailless GFP-Kif18B showing the absence of diffusion in 1 mM ATP. (*C*) Example 2D "top–down" trajectories of GFP-Kif18B-TL coated beads from the video-tracking assay show only directed motions. Data were 10-frame moving averaged. Black arrow indicates the direction of motility. (*D*) Example raw distance vs. time plots of tailless GFP-Kif18B (black) and full-length GFP-Kif18B (other colors) acquired from video tracking. The tailless motor lacks diffusion and moves faster than the full-length motor. (*E*) MSD of GFP-Kif18B-TL in 1 mM ATP calculated from single-molecule fluorescence tracking (blue square) and video tracking (black line). The red curve is a fit to MSD from the single-molecule fluorescence data with MSD = $v^2\tau^2$ + offset, v = 0.166 ± 0.001 μm/s. n = 37. (*F*) Representative kymographs of GFP-Kif18B-TL (*Upper*) in 1 mM ADP and mCh-Kif18B T (*Lower*). Diffusion of the tail domain is much faster than the tailless motor. (*G* and *H*) Two potential models to explain directed-to-diffusion movement transitions. In the first model (*G*), the motor head mediates both directed motions and diffusion. Stochastic interaction between the tail domain and the motor head leads to switching from directed motion to diffusion. In the second model (*H*), diffusion is mediated by interaction of the tail domain with the MT lattice when the motor heads release from the same track. Reattachment of the motor domain results in reversal of motility back to directed motion. Black and blue arrows indicate transitions between directed/diffusive modes of motility and movement directions, respectively. (*I*) MSD of GFP-Kif18B-TL in 1 mM ADP. The red line is a fit to MSD = $2D\tau$ + offset, D = 0.014 ± 0.001 μm^2/s. n = 37. (*J*) MSD of mCh-Kif18B-T. The red line is a fit to MSD = $2D\tau$ + offset, D = 0.676 ± 0.060 μm^2/s. n = 15. (*K*) Dissociation rate constants of three Kif18B variants from the MT lattice. All rates are corrected for photobleaching rates. Values of GFP-Kif18B-FL and GFP-Kif18B-TL are measured in 1 mM ATP.

exhibit a similar activity and that this could facilitate diffusive movement on the MT lattice. To address this possibility, we constructed a tailless version of GFP-Kif18B (GFP-Kif18B-TL) as well as the tail-only domain (mCh-Kif18B-T) fused to mCherry (Fig. 3*A* and Fig. S5 *A* and *B*). At the single-molecule level, the initial intensity distribution of Kif18B-TL was similar to that of Kif18B-FL, indicating that Kif18B-TL exists as a dimer in solution. Interestingly, analysis of the Kif18B tail by analytical ultracentrifugation (AU) shows that the protein exists in both monomeric (66.2%) and dimeric (33.8%) forms (Fig. S5*C*) even though it lacks the coiled-coil region of Kif18B. This result was reflected at the single-molecule level (Fig. S5 *E* and *F*). Importantly, protein concentrations used for AU (micromolar) and the single-molecule fluorescence assay (nanomolar) differed 1,000-fold, strongly suggesting that dimerization of the tail is not an artifact caused by nonspecific protein–protein interactions.

Single-molecule fluorescence measurements with GFP-Kif18B-TL showed only unidirectional motion (Fig. 3*B*). To rule out the possibility that short periods of diffusion were missed due to low spatial and temporal resolution in fluorescence imaging, we examined the motility of tailless Kif18B-bound beads, using video tracking. Two-dimensional trajectories of beads on the MT lattice did not show any sign of diffusion (Fig. 3*C*), confirming that the motor head domain of Kif18B steps unidirectionally along the MT lattice. Position vs. time plots for beads showed not only a lack of diffusive phases but also a faster overall velocity compared with the full-length motor (Fig. 3*D*). Indeed, MSD analysis of the tailless motor fluorescence trajectories revealed the velocity to be 0.166 ± 0.001 $\mu m \cdot s^{-1}$, similar to that of the instantaneous velocity of the full-length motor (Figs. 2*I* and 3*E* and Table 1). These data suggest that the motor head domain of Kif18B steps directionally along the MT lattice and that the tail domain gives rise to its diffusive behavior.

In principle, the tail domain of Kif18B could allow diffusion to take place through one of at least two mechanisms. First, the tail domain could cause the motor head to directly switch its mode of motility, for example by causing the MT-bound motor head to enter an ADP-bound-like state (Fig. 3*G*). Second, the tail domain could remain bound to and diffuse along the MT lattice independent of motor head-track binding (Fig. 3*H*). To discriminate between these possibilities, we first tested whether the Kif18B tail can associate with the MT lattice. In solution, mCh-Kif18B-T bundles MTs polymerized from GMPCPP (Fig. S5*D*). This observation suggests that the tail contains a MT-binding activity and is consistent with our finding that approximately one-third of the protein exists as a dimer in solution (Fig. S5*C*). For single-molecule analysis, we focused on dimers of the Kif18B tail because the dimeric tail represents the native state in the full-length motor. The Kif18B tail associated with MTs and exhibited a k_{off} of 1.36 ± 0.71 s^{-1} (Fig. 3*K*). These data conclusively demonstrate that the tail of Kif18B contains a second MT-binding site. Notably, this second MT-binding site reduces the k_{off} of the motor by ~5-fold (k_{off}: GFP-Kif18B-FL, 0.054 ± 0.014 s^{-1} vs. GFP-Kif18B-TL, 0.28 ± 0.04 s^{-1}) and increases the processivity 1.7-fold (GFP-Kif18B-FL, 0.74 ± 0.22 μm vs. GFP-Kif18B-TL, 0.44 ± 0.09 μm).

We then analyzed diffusion of tailless Kif18B and the Kif18B tail in the presence of ADP, using the single-molecule TIRF assay. Both proteins briefly interacted with MTs and their motility was detectable with a high acquisition rate (17 Hz). MSD analysis revealed that the diffusion constant of the tail, 0.676 ± 0.060 $\mu m^{-2} \cdot s^{-1}$, was much larger than that of the tailless motor, 0.014 ± 0.001 $\mu m^{-2} \cdot s^{-1}$ (Fig. 3 *I* and *J* and Table 1). Importantly, the diffusion constant of tailless Kif18B is similar to that of full-length Kif18B in ADP, suggesting that the interaction between the motor head and the MT limits the diffusion magnitude of the full-length motor. When considered with our observation that the velocity of the tailless motor in ATP is similar to the instantaneous velocity of the full-length motor during directed motion (Table 1), our data favor the model that the motor head executes both directional stepping and diffusion.

We further tested our head-mediated diffusion model by performing MT binding kinetic analysis. In the tail-mediated diffusion model, the diffusive phases of full-length Kif18B coincide with a tail-only bound configuration at the molecular level (Fig. S6*A*). Using measured off rates of the tail and motor head fragments, we analytically calculated mean dwell times of the full-length Kif18B on MTs as a function of kinetic rates and identified parameters for rebinding rates of the tail and head domain that were consistent with the unbinding rate of full-length motors (*SI Text* and Fig. S6 *B* and *C*). Analysis of our simulations revealed that the full-length motor existed in the tail-bound state for only a small fraction of time, <5% (Fig. S6 *D* and *E*). Thus, the head domain of Kif18B itself switches its motility mode to a diffusive phase, facilitated by interaction with the tail domain.

Kif18B Is a Low-Force Motor. Previous single-molecule work on Kip3 and Kif18A showed that these motors exert forces <1 pN (31). To access how much mechanical force Kif18B can generate, we performed an optical trapping assay for full-length Kif18B (Fig. 4*A*). Under a fixed trap configuration, beads coated with full-length Kif18B showed minimal force generation, typically below 1 pN, before snapping back to the trap center (Fig. 4*B*). Because most runs did not show characteristic stalls like kinesin-1 (20), we used the "maximum force" produced by Kif18B to quantify its force-producing capacity (*Materials and Methods*). Kif18B-coated beads frequently showed small displacements around the baseline. Side steps were often observed in Kif18B runs (Fig. 4*B*, *Right*). Because full-length Kif18B spends a significant proportion of its MT-bound time diffusing (Fig. 2*J*), it is possible that switching of movement modes may produce unbinding/slippage that limits the maximum force observed. To exclude this possibility, the same optical trapping assay was applied to tailless Kif18B (Fig. 4*D*). Similar to full-length Kif18B, tailless Kif18B produced forces below 1 pN with a mean maximum force of 0.56 ± 0.02 pN (n = 35). Thus, when considered with previous work (31), our result suggests that kinesin-8 motors generally produce only small amounts of forces.

Table 1. Summary of motile parameters from the MSD analysis

Method of tracking	Protein	Nucleotide	Velocity, *V*, μm/s	Diffusion constant, *D*, $\mu m^2/s$	Relevant figure
Fluorescence tracking	GFP-Kif18B-FL	ATP	0.052 ± 0.003	0.010 ± 0.001	Fig. 2*B*
		ADP	—	0.015 ± 0.001	Fig. 2*D*
	GFP-Kif18B-TL	ATP	0.166 ± 0.001	—	Fig. 3*E*
		ADP	—	0.014 ± 0.001	Fig. 3*I*
	mCh-Kif18B-T	—	—	0.676 ± 0.060	Fig. 3*J*
Video tracking	GFP-Kif18B-FL	ATP	0.045 ± 0.0002	0.0105 ± 0.0004	Fig. S2*B*
		ATP transient directed phase	0.183 ± 0.002	—	Fig. 2*I*

All errors are 95% confidence bounds of the fitted parameters.

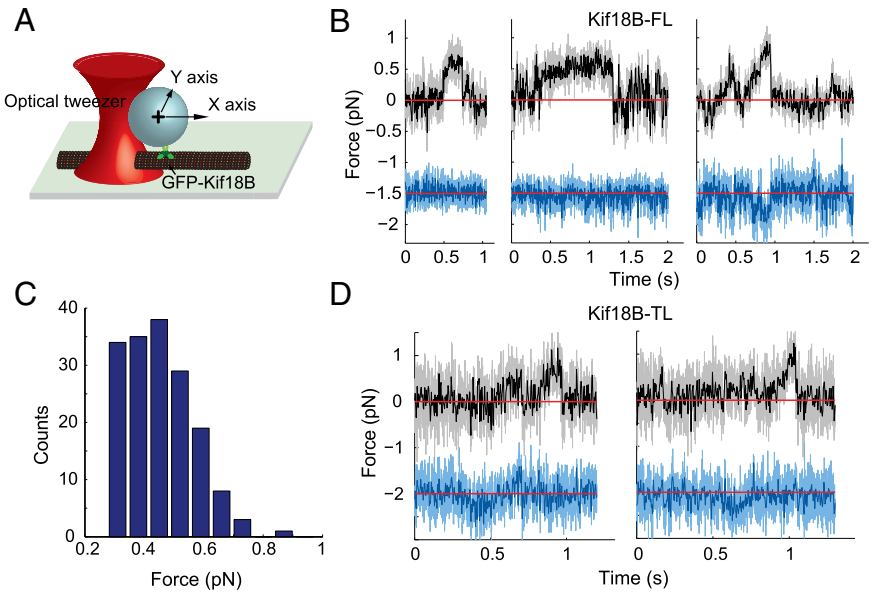

Fig. 4. Kif18B is a low-force motor. (*A*) Schematic diagram of the loaded stationary optical trap assay for Kif18B. As Kif18B walks along the MT, the force exerted on the motor increases, ultimately resulting in unbinding from the MT. (*B*) Representative records of Kif18B-FL–coated beads held in the optical trap along the MT axis [*Upper*, raw data (light gray), decimated to 300 Hz (black)] and the lateral axis [*Lower*, raw data (light blue), decimated to 300 Hz (blue)]. A red line indicates the trap center. Kif18B frequently moves sideway as evidenced by deviation in the lower lateral blue trajectories. (*C*) The distribution of maximal force for Kif18B-FL. The mean maximal force is 0.46 ± 0.01 pN. $n = 170$. (*D*) Representative records of tailless GFP-Kif18B–coated beads in the optical trap assay. Color codes are the same as in *B*.

Two Spatially Resolved Populations of Kif18B Decorate Spindle MT Plus Ends. Our results indicate that the motile properties of Kif18B differ significantly from those of Kip3 and Kif18A. In mammalian cells, Kif18A and Kif18B are also known to bind different MT tracks; Kif18A concentrates on kinetochore fibers (2, 3) whereas Kif18B binds all spindle MTs by binding to EB1 (12, 13). Given these differences, we sought to better define how the motile properties of single Kif18B molecules may influence its distribution at MT plus ends in cells. As a first step, we analyzed the localization of Kif18B in mitotic cells with high-resolution structured illumination microscopy (SIM). Consistent with previous reports, we observed that Kif18B localizes to the plus ends of most spindle MTs, overlapping with EB1 (class I, Fig. 5 *A* and *B*) (12, 13). Careful inspection of the images, however, revealed that a subset of MT-associated Kif18B formed spots slightly displaced from EB1 comets (class II, Fig. 5 *A* and *B*). GFP-tagged Kif18B imaged in fixed cells without immunostaining showed an identical pattern (Fig. S7*A*), indicating that localization of Kif18B to the extreme plus end is not an immunostaining artifact. We measured the displacement of Kif18B from EB1 comets, using subpixel analysis of images collected by SIM (Fig. S7*B* and *Materials and Methods*), and found that the motor superseded EB1 by 189 ± 123 nm (mean ± SD; $n = 25$ MT plus ends; Fig. 5*C*). This distance corresponds to roughly 24 tubulin subunits on a 13-protofilament MT.

Kif18B joins a growing list of proteins that localize to the MT plus-end terminus, the best characterized of which is ch-TOG (32, 33). To determine whether ch-TOG and Kif18B occupy similar or distinct regions of the plus end, we compared the plus-end distributions of the two proteins in fixed mitotic cells. We first analyzed the distance between ch-TOG and EB1 in interphase cells because this value has been measured previously. In agreement with published data (33), our analysis shows that ch-TOG is positively displaced from EB1 by 140 ± 108 nm ($n = 10$ MT plus ends; Fig. S7*C*). The separation during mitosis is 165 ± 111 nm ($n = 25$ MT plus ends; Fig. 5 *D*–*F*), which is not significantly different from interphase. The spatial distributions of Kif18B and ch-TOG at MT plus ends during mitosis are well aligned relative to EB1 (Fig. 5*G*), supporting the idea that Kif18B, like cH-TOG, can reach the very extreme plus end of MTs.

Discussion

The well-studied kinesin-8 motors Kip3 and Kif18A exhibit three properties that distinguish them from other members of the kinesin superfamily: (*i*) They translocate for exceptionally long distances along the MT lattice toward the plus end (8, 10, 15, 16), (*ii*) they exhibit long dwell times at the MT plus end (8–10, 18), and (*iii*) they modulate MT plus-end dynamics (7–10, 34). Despite its classification as a kinesin-8, our data show that Kif18B is markedly different from Kip3 and Kif18A. Compared with Kip3 and Kif18A, Kif18B exhibits ∼10-fold reduced processivity and a >50-fold reduction in plus-end dwell time. These data clarify the requirement of EB1 binding for Kif18B to target spindle MT plus ends (12, 13); traversing <1 μm per round of binding to the MT track, Kif18B would not be expected to use its motility to accumulate at plus ends of astral MTs, which average ∼6 μm in length. Whether Kif18B can directly regulate MT plus-end dynamics is not known, but recent work showing that the Kif18B motor domain can drive chromosome congression strongly suggests that it does (14).

The high processivities of Kip3 and Kif18A are enabled in part by the presence of a second MT-binding site in their tail domains, which tethers these motors to the MT track (10, 15, 16, 35). The Kif18B tail, on the other hand, was thought to function primarily as an EB1-binding module (12, 13). Interestingly, our work demonstrates that the Kif18B tail also contains a second MT-binding site and that this activity imparts a 1.7-fold increase in processivity. These data suggest that the functional organization of Kif18A/Kip3 and Kif18B is generally conserved and that sequence alterations among kinesin-8 family members produce significantly different motile properties. Amino acid substitutions within the motor domains of Kif18A and Kif18B, in particular, are likely to contribute to differences in their processivities. This possibility is supported by the observations that tailless Kif18A

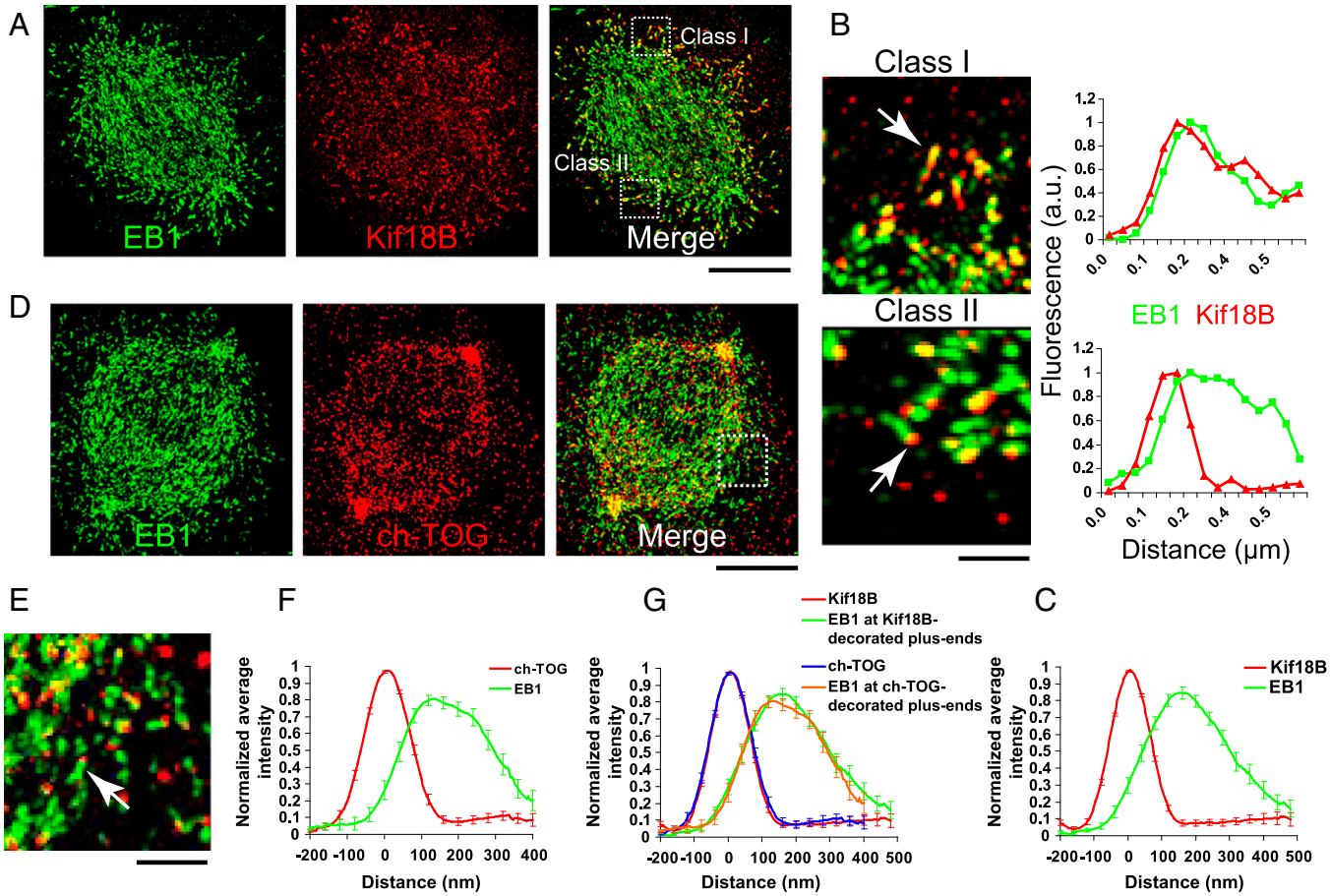

Fig. 5. Kif18B exhibits a complex distribution at the plus ends of spindle MTs. (*A*) Kif18B (red) and EB1 (green) distributions in a metaphase HeLa cell determined by structured illumination microscopy. The class I and class II regions are indicated and enlarged in *B*. (Scale bar, 5 μm.) (*B*) Kif18B exhibits two classes of localization at the MT plus end. The indicated comets (arrows) were used to generate linescans. (Scale bar, 1 μm.) (*C*) Average intensity profiles of Kif18B (red) and EB1 (green) during mitosis by SIM (n = 25 comets). Alignment of multiple comet profiles was performed with subpixel accuracy before being averaged (Fig. S7*B*) (*Materials and Methods*). The error bars are SEM. (*D*) ch-TOG (red) and EB1 (green) distributions in a metaphase HeLa cell. (Scale bar, 5 μm.) The indicated regions are enlarged in *E*. (*E*) An example comet for EB1 and ch-TOG is indicated with a white arrow. (Scale bar, 1 μm.) (*F*) Average intensity profiles of ch-TOG (red) and EB1 (green) during mitosis (n = 25 comets). The same method of alignment and averaging was used as in *C*. The error bars are SEM. (*G*) Display of *C* and *F* together: Kif18B in red, EB1 at the Kif18B-decorated plus ends in green, ch-TOG in blue, and EB1 at the ch-TOG–decorated plus ends in orange.

exhibits robust MT binding and high processivity in buffers exceeding physiological ionic strength (10), whereas the dwell time of tailless Kif18B on the MT lattice is low even in BRB80 alone (Fig. 3*K*).

Kip3 and Kif18A possess a "weakly bound slip state" lasting for ∼10 ms, observed under load (31). Our data show that Kif18B also switches its motile mode between directed movement and diffusion yet differs drastically from Kip3 and Kif18A in that it spends the majority of time in diffusion, a similar behavior to that reported for CENP-E (36) and Eg5 (37). In the presence of ATP, diffusive motility is observed with full-length Kif18B but not the tailless motor under our experimental timescale, suggesting that the tail significantly promotes diffusion. Moreover, a short temporal fraction in the tail-bound configuration (Fig. S6) as well as a high diffusion constant of the tail fragment (Fig. 3*J*) compared with the full-length motor indicates that the motor head of Kif18B itself switches its motility mode, facilitated by the tail domain. Interestingly, kinesin-1 autoinhibition is achieved by interaction of a sequence (QIAKPIRP) contained in its C-terminal tail domain with the motor head, preventing ADP release (38–40). It is possible that the tail of Kif18B similarly affects its motor heads, an idea consistent with the observation that tailless Kif18B diffuses in the presence of ADP. It is worth noting that the motile properties of Kif18A are also modulated by its tail; full-length Kif18A pauses frequently, leading to an approximately twofold reduction in overall velocity compared with tailless Kif18A (10). A tail-based autoinhibition mechanism may be conserved between Kif18A and Kif18B, but the consequence of this regulation—i.e., diffusion vs. pausing—may depend on the affinity of ADP-bound motor heads for the MT lattice, as discussed above.

Although the physiological relevance of Kif18B's unique motile properties remains unclear, previous work has shown that Kif18B prevents astral MT overgrowth in the mitotic spindle (12, 13). Our SIM data place Kif18B at the extreme plus end of the MT, an ∼200-nm stretch of tubulin subunits that was previously known to harbor only ch-TOG/XMAP215 (32, 33) and TACC3 (41). This location is ideal for Kif18B to have a direct effect on MT plus-end dynamics, but raises the question of how it gets there. Our MSD analysis shows that the overall velocity of Kif18B is ∼3 μm·min^{-1}, a speed approximately fivefold slower than the growth rate of MTs during mitosis (42). Because mammalian cells are maintained at temperatures higher than those used in our studies, one possibility is that our velocity measurements underestimate the speed of Kif18B's motility in vivo. In light of our data, however, a second possibility is that

diffusion enables the occasional capture of a growing MT plus end by Kif18B, even in the case where the growth rate of MTs is faster than the average stepping velocity of Kif18B. For example, diffusion-based transport with a diffusion constant similar to Kif18B (0.015 $\mu m^{-2} \cdot s^{-1}$) outpaces the growth rate of MTs, v, of 12.8 $\mu m \cdot min^{-1}$ for any distance shorter than ~0.14 μm, calculated as $2D/v$. A complication of this model is that diffusion along the MT lattice is, by definition, bidirectional. Diffusive motion toward the minus end would negatively impact the plus-end catch rate. Two factors can address this complication. First, the ATPase-directed transport activity of the Kif18B motor domain biases the motion of Kif18B molecules toward the MT plus end. Second, excessive backward movements may be prevented by rebinding of the motor to EB1 and periodically transitioning into an active transport phase. Future work is needed to better understand how motility, diffusion, and EB1 binding affect MT tip targeting by Kif18B.

Materials and Methods

Molecular Biology and Baculovirus Construction. pGEX6P-1-Kif18B-CT, which encodes the C-terminal tail of human Kif18B fused to GST, was constructed by PCR amplification of codons 575–842 and subcloning into the BamHI and EcoRI sites of pGEX6P-1 (Amersham). To create pFastBac1-GFP-Kif18B-His10, the GFP-Kif18B coding region was PCR amplified from pEGFP-C2-Kif18B (a gift from Wankee Kim, Institute for Medical Sciences, School of Medicine, Ajou University, Suwon, South Korea) (43) with a 3′ oligonucleotide that inserts 10 histidine codons in between the last Kif18B residue and the termination codon. This fragment was subcloned into the BamHI and SalI sites of pFastBac1 (Invitrogen) to construct pFastBac1-GFP-Kif18B-His10. A baculovirus that expresses GFP-Kif18B-FL-His10 was generated using the Bac-to-Bac system (Invitrogen). A baculovirus that expresses GFP-Kif18B-TL was similarly prepared. For expression of mCh-Kif18B-T in *Escherichia coli*, a pET15b-mCherry-Kif18B-T vector was constructed by isothermal assembly of mCherry and Kif18B-C268 sequences into pET15b restricted with NdeI and XhoI.

Protein Expression and Purification. GST-Kif18B-CT was expressed in *E. coli* and purified using standard techniques. GFP-Kif18B-FL and GFP-Kif18B-TL were expressed in Sf-9 cells and purified using methods described previously (9) except that 500 mM imidazole was used in the elution step and the protein was not subjected to size exclusion chromatography. Instead, following elution from Ni^{++}-NTA agarose (Qiagen), the motor was immediately buffer exchanged into 10 mM K-Hepes, pH 7.7, 300 mM KCl, 1 mM DTT, 0.1 mM MgATP, using a PD-10 column (GE Healthcare). The motor concentration was measured by Bradford assays and calculated assuming that GFP-Kif18B-FL and GFP-Kif18B-TL exist as dimers in solution. Single-molecule microscopy confirmed that the motor is monodispersed and behaves as a dimer in solution. mCh-Kif18B-T was expressed in BL21 cells. Cells were resuspended in lysis buffer [10 mM imidazole, pH 7.8, 500 mM NaCl, 1% IGEPAL CA-630, 5 mM β-mercaptoethanol, and protease inhibitors (1 mM phenylmethylsulfonyl fluoride; 1 mM benzamidine; and 10 μg/mL each of leupeptin, pepstatin, and chymostatin)] containing 1 mg/mL lysozyme. The lysate was sonicated and clarified by centrifugation at 35,000 rpm for 1 h in a Ti 50.2 rotor (Beckman). Supernatants were incubated with ~3 mL of Ni-NTA resin (Qiagen) for 1 h at 4 °C and then washed extensively with lysis buffer lacking IGEPAL CA-630 and protease inhibitors. Proteins were eluted into 310 mM imidazole, 500 mM NaCl, 1 mM DTT and peak fractions were pooled. After buffer change into 10 mM K-Hepes, pH 7.7, 300 mM KCl, 1 mM DTT using a PD-10 column (GE Healthcare), all eluates were subjected to size exclusion chromatography on a Hiload 16/60 Superdex 200 preparatory grade column (GE Healthcare).

Analytical Ultracentrifugation. Purified mCh-Kif18B-T was run in an Optima XLI ultracentrifuge (Beckman Coulter) equipped with a four-hole An-60 Ti rotor at 42,000 rpm at 4 °C. Samples were loaded into double-sector cells (path length of 1.2 cm) with charcoal-filled Epon centerpieces and sapphire windows. The buffer used for AU was 10 mM K-Hepes, pH 7.7, 300 mM KCl, 1 mM DTT. Sedfit (version 12.0) was used to analyze velocity scans, using every 4 scans from a total of 250 scans. Approximate size distributions were determined for a confidence level of $P = 0.95$, a resolution of $n = 300$, and sedimentation coefficients between 0 S and 15 S. A Bayesian analysis was used to determine the approximate molecular weight of each peak.

Generation of Kif18B Antibodies. GST-Kif18B-CT was used to immunize rabbits (Cocalico). Kif18B antibodies were affinity purified by passing anti–GST-depleted serum over Affi-Gel 10 coupled to the immunogen. Antibodies were dialyzed against PBS, aliquoted, and frozen in liquid N_2.

Cell Culture and Transfection. HeLa "Kyoto" cells were cultured in DMEM containing 10% (vol/vol) FCS plus antibiotics and were plated onto 12-mm glass coverslips for ~24 h before transfection. Transfection was performed using Lipofectamine 2000 (Invitrogen) according to the manufacturer's instructions. Cells were processed for immunofluorescence 24 h posttransfection.

Immunofluorescence, Deconvolution, and Image Analysis. HeLa cells were fixed with methanol at −20 °C for 10 min. Cells were labeled with the following primary antibodies: rabbit anti-Kif18B (1 μg/mL), mouse anti-EB1 (1:500; BD Transduction Laboratories), and goat anti-ch-TOG (1:1,000; Santa Cruz) for 45 min at room temperature. Anti-mouse, anti-rabbit, and anti-goat secondary antibodies conjugated to Alexa 488 or Alexa 594 (Invitrogen) were used at 1:1,000 for 30 min. DNA was counterstained with 5 μg/mL Hoechst 33342. Stained cells were mounted in Prolong (Invitrogen) and imaged using a Deltavision Core equipped with a CCD camera and 100× 1.4 NA objective (Applied Precision). Z stacks were taken at 200-nm intervals and deconvolved using softWoRx image restoration software (Applied Precision). Alternatively, specimens were imaged using OMX (Applied Precision) or N-SIM (Nikon) superresolution microscopes. For 3D SIM, images were acquired at 125-nm intervals as previously described (44) and processed using softWoRx or NIS Elements (Nikon). To measure the distance between Kif18B and EB1 in class II plus ends, we used SIM reconstructed images with both proteins present in the same focal plane. The intensity profile for each comet was generated by linescans in ImageJ and then background subtracted before being normalized with the peak intensity. A Gaussian fit was performed to the normalized intensity of the Kif18B profile to locate a peak position in subpixel resolution. The alignment of distinct comets with subpixel precision was achieved by linear interpolation of original profiles into 10-fold finer pixels such that the peak positions of the Kif18B population were overlaid at the origin. The aligned profiles were then averaged to generate a normalized average intensity plot.

Single-Molecule Fluorescence Tracking and Analysis. Single-molecule imaging, localization, and analyses were performed essentially as previously reported (45). Motility of single Kif18B molecules was measured using a heavily modified inverted microscope, a 100× 1.49 NA TIRF objective, an EMCCD camera, and a 488/532-nm two-color TIRF illumination system (45). Single-molecule experiments were performed in flow cells with biotinylated GMPCPP MTs, grown from purified bovine brain tubulin labeled with rhodamine, linked to biotin–PEG-coated coverslips via streptavidin. TIRF experiments were carried out in BRB80 containing 1 mM DTT, 1 mg/mL casein, 1 mM ATP (1 mM ADP to monitor the diffusional behavior only), and an oxygen scavenging system (5 mg/mL β-D-glucose, 0.25 mg/mL glucose oxidase, and 0.03 mg/mL catalase). For measurements of motility, 1 nM GFP-Kif18B was added to the assay buffer and frames were collected at one frame per second. To increase the lifetime of GFP fluorescence, the excitation laser was modulated at 1 Hz and synchronized with data acquisition. One hundred-millisecond exposures were used in most recordings. The localization accuracy was quantified with variances in tracked positions of surface-immobilized molecules. To observe transient motility of GFP-Kif18B-TL and mCh-Kif18B-T, the acquisition rate was increased to 17 Hz. Images were analyzed using custom MATLAB software and the validity of each track was confirmed by visual inspection. The MSD of each single-molecule trace was computed and then averaged over all traces. The diffusion coefficient and drift velocity were then determined by performing weighted fits with appropriate models described in the main text to the first 5 ~ 8 points of the MSD because in general the error of the MSD quickly increases when τ becomes large (46). Kymographs and dual color images were generated from representative GFP-Kif18B motors in ImageJ 1.44p (National Institutes of Health).

Video-Tracking and Optical Trapping Assay. Streptavidin-conjugated beads (0.44 μm diameter; Spherotech) were coated with biotinylated pentahistidine antibody (Qiagen) through 1-h incubation at 4 °C. Excess antibody was removed by centrifuging the bead solution and resuspending it in PBS four times. The appropriate Kif18B construct was diluted and mixed with beads in BRB80 with 1 mM DTT, 1 mg/mL casein, 20 μM Taxol (paclitaxel), and 1 mM ATP and incubated for 1 h at 4 °C. After the oxygen-scavenging system was added to the Kif18B-coated bead solution, the beads were introduced into the flow cell with Taxol-stabilized MTs immobilized on the poly(L-lysine)–coated etched coverslip. To ensure the single-molecule limit, the protein–bead ratio was adjusted so that fewer than half of the beads captured by the optical trap and tested on microtubules showed binding. The video-tracking assay was performed by trapping a freely diffusing bead and placing it on a

microtubule. The trap was immediately shuttered upon binding of the bead and the bead motion was recorded at 30 Hz, using video-enhanced DIC. Custom-built MATLAB scripts based on a cross-correlation method (19) were used to track positions of beads. The tracking programs were tested using immobilized beads on a glass surface and moving a piezo stage at predetermined step sizes. The optical trapping measurements were performed in a stationary optical tweezers instrument with separate trapping and detection systems. The setup and calibration procedures are described in detail elsewhere (47). Briefly, a 1.5-W Nd:YVO4 laser (1,064 nm) was expanded and coupled into an inverted microscope with a 100×/1.3 NA oil-immersion objective. Displacements from the trap center of beads were recorded at 3 kHz, antialias filtered at 1.5 kHz. Trap stiffnesses ranging from 0.01 pN/nm to 0.02 pN/nm were used for all experiments. Motility data were analyzed using custom-built MATLAB scripts. The maximum forces were detected using the criteria force $\geq$ 0.2 pN, snapback velocity $\geq$ 1,000 nm/s, run lasting longer than 33 ms, and a snapback to baseline.

Detection of Transient Directed Motions. Detection of transient directed phases from diffusion was carried out based on a speed correlation index (SCI) (29). Briefly, the SCIs along trajectories were computed with an averaging window of size L, 44 time points (1.47 s). The size of the window was chosen to reduce the Brownian noise, yet allow the acquisition of local information. A minimal possible value for L is one where a distance traveled via directed motions is comparable to one from diffusion, $L \sim 2D/v^2t$, where t is a time increment. With measured values for Kif18B, the minimum L is 27 frames and we acquired similar results with L between 30 frames and 44 frames. To objectively discriminate transient directed motions from diffusion, we simulated 400 traces from Brownian motion, computed SCIs, and constructed a curve with thresholds $p(H_c,T_c)$, where the estimated probability of observing a SCI higher than H_c for a time longer than T_c only due to stochastic fluctuation is below 5% (29). Only events with SCIs above H_c that lasted longer than T_c are considered as directed motions.

Kinetic Analysis for Kif18B-FL Binding to MTs. A detailed description for the theoretical calculation and computer simulations of Kif18-FL binding kinetics to MTs is provided in *SI Text*.

MT Gliding Assays and mCh-Kif18B-T–MT Interaction Assays. Motility assays were performed and analyzed as described previously (9). To visualize the interaction of mCh-Kif18B-T with MTs in vitro, 900 ng of protein was incubated with GMPCPP MTs (250 nM tubulin) in BRB80, 50 mM KCl, 1 mM DTT at room temperature. Reactions were monitored by squashing 2 μL underneath an 18 × 18-mm coverslip and observing them by fluorescence microscopy through a 100× 1.4 NA objective (Nikon).

ACKNOWLEDGMENTS. We thank Wankee Kim, William R. Hesse, and Irina Kaverina for reagents and members of the P. Ohi laboratory for critical reading of the manuscript. We thank Wonmuk Hwang for helpful discussions. This work was supported by National Institutes of Health (NIH) Grants R01GM087677 (to M.J.L.) and R01GM086610 (to R.O.). M.J.L. was also supported by grants from the National Science Foundation (MCB-1330792) and the Singapore–Massachusetts Institute of Technology Alliance for Research and Technology program. Y.S. acknowledges a Samsung Scholarship from the Samsung Foundation of Culture. Structured illumination microscopy data were collected on N-SIM and OMX microscopes at Nikon and Applied Precision, respectively, and an OMX microscope located in the Core Imaging Shared Resource at Vanderbilt University Medical Center purchased with NIH Grant 1S10OD012324 to Matthew J. Tyska. R.O. is a Scholar of the Leukemia and Lymphoma Society.

1. DeZwaan TM, Ellingson E, Pellman D, Roof DM (1997) Kinesin-related KIP3 of Saccharomyces cerevisiae is required for a distinct step in nuclear migration. *J Cell Biol* 138(5):1023–1040.
2. Mayr MI, et al. (2007) The human kinesin Kif18A is a motile microtubule depolymerase essential for chromosome congression. *Curr Biol* 17(6):488–498.
3. Stumpff J, von Dassow G, Wagenbach M, Asbury C, Wordeman L (2008) The kinesin-8 motor Kif18A suppresses kinetochore movements to control mitotic chromosome alignment. *Dev Cell* 14(2):252–262.
4. Zhu C, et al. (2005) Functional analysis of human microtubule-based motor proteins, the kinesins and dyneins, in mitosis/cytokinesis using RNA interference. *Mol Biol Cell* 16(7):3187–3199.
5. Niwa S, et al. (2012) KIF19A is a microtubule-depolymerizing kinesin for ciliary length control. *Dev Cell* 23(6):1167–1175.
6. Su X, Ohi R, Pellman D (2012) Move in for the kill: Motile microtubule regulators. *Trends Cell Biol* 22(11):567–575.
7. Gupta ML, Jr, Carvalho P, Roof DM, Pellman D (2006) Plus end-specific depolymerase activity of Kip3, a kinesin-8 protein, explains its role in positioning the yeast mitotic spindle. *Nat Cell Biol* 8(9):913–923.
8. Varga V, et al. (2006) Yeast kinesin-8 depolymerizes microtubules in a length-dependent manner. *Nat Cell Biol* 8(9):957–962.
9. Du Y, English CA, Ohi R (2010) The kinesin-8 Kif18A dampens microtubule plus-end dynamics. *Curr Biol* 20(4):374–380.
10. Stumpff J, et al. (2011) A tethering mechanism controls the processivity and kinetochore-microtubule plus-end enrichment of the kinesin-8 Kif18A. *Mol Cell* 43(5):764–775.
11. Stumpff J, Wagenbach M, Franck A, Asbury CL, Wordeman L (2012) Kif18A and chromokinesins confine centromere movements via microtubule growth suppression and spatial control of kinetochore tension. *Dev Cell* 22(5):1017–1029.
12. Stout JR, et al. (2011) Kif18B interacts with EB1 and controls astral microtubule length during mitosis. *Mol Biol Cell* 22(17):3070–3080.
13. Tanenbaum ME, et al. (2011) A complex of Kif18b and MCAK promotes microtubule depolymerization and is negatively regulated by Aurora kinases. *Curr Biol* 21(16):1356–1365.
14. Kim H, Fonseca C, Stumpff J (2014) A unique kinesin-8 surface loop provides specificity for chromosome alignment. *Mol Biol Cell* 25(21):3319–3329.
15. Mayr MI, Storch M, Howard J, Mayer TU (2011) A non-motor microtubule binding site is essential for the high processivity and mitotic function of kinesin-8 Kif18A. *PLoS ONE* 6(11):e27471.
16. Su X, et al. (2011) Mechanisms underlying the dual-mode regulation of microtubule dynamics by Kip3/kinesin-8. *Mol Cell* 43(5):751–763.
17. Wargacki MM, Tay JC, Muller EG, Asbury CL, Davis TN (2010) Kip3, the yeast kinesin-8, is required for clustering of kinetochores at metaphase. *Cell Cycle* 9(13):2581–2588.
18. Varga V, Leduc C, Bormuth V, Diez S, Howard J (2009) Kinesin-8 motors act cooperatively to mediate length-dependent microtubule depolymerization. *Cell* 138(6):1174–1183.
19. Gelles J, Schnapp BJ, Sheetz MP (1988) Tracking kinesin-driven movements with nanometre-scale precision. *Nature* 331(6155):450–453.
20. Svoboda K, Block SM (1994) Force and velocity measured for single kinesin molecules. *Cell* 77(5):773–784.
21. Coombes CE, Yamamoto A, Kenzie MR, Odde DJ, Gardner MK (2013) Evolving tip structures can explain age-dependent microtubule catastrophe. *Curr Biol* 23(14):1342–1348.
22. Kolomeisky AB, Fisher ME (2007) Molecular motors: A theorist's perspective. *Annu Rev Phys Chem* 58:675–695.
23. Nishikawa M, Takagi H, Shibata T, Iwane AH, Yanagida T (2008) Fluctuation analysis of mechanochemical coupling depending on the type of biomolecular motors. *Phys Rev Lett* 101(12):128103.
24. Svoboda K, Mitra PP, Block SM (1994) Fluctuation analysis of motor protein movement and single enzyme kinetics. *Proc Natl Acad Sci USA* 91(25):11782–11786.
25. Okada Y, Hirokawa N (1999) A processive single-headed motor: Kinesin superfamily protein KIF1A. *Science* 283(5405):1152–1157.
26. Kwok BH, et al. (2006) Allosteric inhibition of kinesin-5 modulates its processive directional motility. *Nat Chem Biol* 2(9):480–485.
27. Roostalu J, et al. (2011) Directional switching of the kinesin Cin8 through motor coupling. *Science* 332(6025):94–99.
28. Lang MJ, Asbury CL, Shaevitz JW, Block SM (2002) An automated two-dimensional optical force clamp for single molecule studies. *Biophys J* 83(1):491–501.
29. Bouzigues C, Dahan M (2007) Transient directed motions of GABA(A) receptors in growth cones detected by a speed correlation index. *Biophys J* 92(2):654–660.
30. Smith DA, Simmons RM (2001) Models of motor-assisted transport of intracellular particles. *Biophys J* 80(1):45–68.
31. Jannasch A, Bormuth V, Storch M, Howard J, Schäffer E (2013) Kinesin-8 is a low-force motor protein with a weakly bound slip state. *Biophys J* 104(11):2456–2464.
32. Maurer SP, et al. (2014) EB1 accelerates two conformational transitions important for microtubule maturation and dynamics. *Curr Biol* 24(4):372–384.
33. Nakamura S, et al. (2012) Dissecting the nanoscale distributions and functions of microtubule-end-binding proteins EB1 and ch-TOG in interphase HeLa cells. *PLoS ONE* 7(12):e51442.
34. Gardner MK, Zanic M, Gell C, Bormuth V, Howard J (2011) Depolymerizing kinesins Kip3 and MCAK shape cellular microtubule architecture by differential control of catastrophe. *Cell* 147(5):1092–1103.
35. Weaver LN, et al. (2011) Kif18A uses a microtubule binding site in the tail for plus-end localization and spindle length regulation. *Curr Biol* 21(17):1500–1506.
36. Gudimchuk N, et al. (2013) Kinetochore kinesin CENP-E is a processive bi-directional tracker of dynamic microtubule tips. *Nat Cell Biol* 15(9):1079–1088.
37. Kapitein LC, et al. (2008) Microtubule cross-linking triggers the directional motility of kinesin-5. *J Cell Biol* 182(3):421–428.
38. Dietrich KA, et al. (2008) The kinesin-1 motor protein is regulated by a direct interaction of its head and tail. *Proc Natl Acad Sci USA* 105(26):8938–8943.
39. Hackney DD, Stock MF (2008) Kinesin tail domains and Mg2+ directly inhibit release of ADP from head domains in the absence of microtubules. *Biochemistry* 47(29):7770–7778.
40. Kaan HY, Hackney DD, Kozielski F (2011) The structure of the kinesin-1 motor-tail complex reveals the mechanism of autoinhibition. *Science* 333(6044):883–885.
41. Nwagbara BU, et al. (2014) TACC3 is a microtubule plus end-tracking protein that promotes axon elongation and also regulates microtubule plus end dynamics in multiple embryonic cell types. *Mol Biol Cell* 25(21):3350–3362.

42. Rusan NM, Fagerstrom CJ, Yvon AM, Wadsworth P (2001) Cell cycle-dependent changes in microtubule dynamics in living cells expressing green fluorescent protein-alpha tubulin. *Mol Biol Cell* 12(4):971–980.
43. Lee YM, et al. (2010) Cell cycle-regulated expression and subcellular localization of a kinesin-8 member human KIF18B. *Gene* 466(1–2):16–25.
44. Schermelleh L, et al. (2008) Subdiffraction multicolor imaging of the nuclear periphery with 3D structured illumination microscopy. *Science* 320(5881): 1332–1336.
45. Shin Y, et al. (2009) Single-molecule denaturation and degradation of proteins by the AAA+ ClpXP protease. *Proc Natl Acad Sci USA* 106(46):19340–19345.
46. Bouzigues C, Lévi S, Triller A, Dahan M (2007) Single quantum dot tracking of membrane receptors. *Methods Mol Biol* 374:81–91.
47. Khalil AS, et al. (2008) Kinesin's cover-neck bundle folds forward to generate force. *Proc Natl Acad Sci USA* 105(49):19247–19252.
48. Cao J, Silbey RJ (2008) Generic schemes for single-molecule kinetics. 1: Self-consistent pathway solutions for renewal processes. *J Phys Chem B* 112(41):12867–12880.
49. Ninio J (1987) Alternative to the steady-state method: Derivation of reaction rates from first-passage times and pathway probabilities. *Proc Natl Acad Sci USA* 84(3):663–667.
50. Singh MP, Mallik R, Gross SP, Yu CC (2005) Monte Carlo modeling of single-molecule cytoplasmic dynein. *Proc Natl Acad Sci USA* 102(34):12059–12064.